Obscuring Environment and X-Ray Variability of Compact Symmetric Objects Unveiled with XMM-Newton and NuSTAR

Małgosia Sobolewska[1] , Aneta Siemiginowska[1] , Giulia Migliori[2] , Luisa Ostorero[3] , Łukasz Stawarz[4] , and Matteo Guainazzi[5]

[1] Center for Astrophysics | Harvard & Smithsonian, 60 Garden Street, Cambridge, MA 02138, USA; msobolewska@cfa.harvard.edu
[2] INAF, Istituto di Radio Astronomia di Bologna, Via P. Gobetti 101, I-40129 Bologna, Italy
[3] Dipartimento di Fisica—Università degli Studi di Torino and Istituto Nazionale di Fisica Nucleare (INFN), Via P. Giuria 1, 10125 Torino, Italy
[4] Astronomical Observatory, Jagiellonian University, ul. Orla 171, 30-244 Kraków, Poland
[5] European Space Research and Technology Centre (ESA/ESTEC), Kepleriaan 1, 2201 AZ, Noordwijk, The Netherlands

Abstract

Compact symmetric objects (CSOs) show radio features such as jets, lobes, and hot spots, which are contained within their host galaxies, and likely represent a recent radio activity. A subpopulation of CSOs with high intrinsic X-ray column densities has been inferred from shallow, soft X-ray band exposures, and observed to cluster in the linear radio size versus 5 GHz radio power plane, which suggests that a dense circumnuclear medium may dramatically influence the growth of compact radio structures. Here, we report on the first detection of two CSOs, 2021+614 and J1511+0518, at energies above 10 keV with NuSTAR. We model the NuSTAR data jointly with the new XMM-Newton data of J1511+0518, and with the archival XMM-Newton data of 2021+614. A toroidal reprocessor model fits the data well and allows us to robustly confirm the X-ray properties of the CSO absorbers and continuum. In both sources, we find intrinsic X-ray absorbing column densities in excess of 10^{23} cm^{-2}, hard photon indices of the primary emission, $\Gamma \sim 1.4$–1.7, Fe Kα line emission, and variability of the intrinsic X-ray flux density on the timescale of years. The studied X-ray continua are dominated by the primary power-law emission at energies above 3 keV, and by the scattered component at energies below 3 keV. An additional soft X-ray component, modeled with a hot, collisionally ionized plasma with temperature $kT \sim 1$ keV, is required by the XMM-Newton data in J1511+0518, which is corroborated by the tentative evidence for the extension in the archival Chandra image of the source.

1. Introduction

We study broadband X-ray emission of extragalactic radio sources belonging to the class of compact symmetric objects (CSOs). CSOs are defined by their radio structures with a symmetrical morphology, suggesting that they are viewed from a direction perpendicular to the jet axis, and have a compact projected radio sizes $\lesssim$1 kpc (see Readhead et al. 2021, for the overview of the CSO properties). CSOs were reported to expand rapidly into the interstellar medium (ISM), showing an average advance velocity of their radio hotspots of $v = 0.1c$ (see the recent review by O'Dea & Saikia 2021, and references therein; Kawakatu et al. 2008). A simple kinematic argument based on high expansion velocities and compact sizes supports the idea that the radio structures of CSOs are young, with ages between a few tens and a few thousands of years (e.g., Snellen et al. 2000; Kunert-Bajraszewska et al. 2010; An & Baan 2012, and references therein).

In the recent years, multiwavelength advances led to discoveries of clumps of cold matter with unsettled kinematics within the innermost few tens to a few hundreds of parsecs from the center of CSOs (e.g., Maccagni et al. 2016, 2018; Santoro et al. 2018; Papachristou et al. 2021). This refueled the

idea that some CSO jets may not expand freely due to a dense environment, which could contribute to their radio compactness (e.g., van Breugel et al. 1984; Bicknell et al. 1997; Sutherland & Bicknell 2007; Callingham et al. 2015, 2017; Tingay et al. 2015). Understanding the interplay between the gas reservoir available in the innermost vicinity of a supermassive black hole in active galactic nucleus (AGN), the mechanism of launching a radio jet, and the interaction of jets with the ISM, is of utter importance for understanding the AGN-galaxy feedback process. The CSOs are ideal targets to study such a process on the smallest, parsec scales.

The goal of our X-ray study is to constrain the intrinsic X-ray column density in the two selected CSOs, and to estimate the potential of their environment to either confine or power their radio jets. The sources were selected from the Sobolewska et al. (2019a; hereafter S19a) sample. S19a considered CSOs with measured expansion velocities of their radio structures, and good quality X-ray spectra, provided by either X-ray Multi-Mirror Mission (XMM-Newton) or Chandra. For the resulting sample of 24 sources, they showed that CSOs affected by absorbers with intrinsic X-ray equivalent hydrogen column density $N_H \gtrsim 10^{23}$ cm^{-2} (hereafter heavily X-ray absorbed CSOs) and CSOs with $N_H \lesssim 10^{23}$ cm^{-2} appear to occupy separate regions in the three-dimensional parameter space defined by the 5 GHz radio luminosity, the projected radio linear size (LS), and intrinsic N_H. They argued that this separation could be due to the heavily X-ray absorbed CSOs

having smaller radio sizes than the CSOs with a low intrinsic N_H and a comparable 5 GHz radio power. Alternatively, they pointed out that the heavily X-ray absorbed CSOs could be more radio luminous than X-ray CSOs with a low intrinsic N_H and a comparable radio size. Both scenarios underline a key role of the surrounding high density environment in shaping the appearance of compact radio jets.

On the one hand, a high density, inhomogeneous ISM in the central region of the host galaxy could prevent a compact radio source from expanding freely for a large fraction of its life (e.g., Sutherland & Bicknell 2007). If such an early phase is followed by a phase where the expansion velocity increases, the estimate of the kinematic age of the source would return a lower limit to the actual source age, based on measurement of the present-day expansion velocity and on the assumption of constant expansion speed over the source lifetime. A large discrepancy between a lower kinematic age and a high spectral age is an indication that the above scenario may hold for the source.

On the other hand, a radio source born in a dense environment could appear more radio luminous than a source born in a low density environment. This could arise as a consequence of a dense environment being able to sustain a higher mass accretion rate, leading to an increased jet power, and hence an increased radio luminosity.

Broadband X-ray constraints, including the >10 keV energy band, on the intrinsic X-ray continua and Fe Kα line radiative output are a key to robust measurements of the intrinsic column densities in AGN. The S19a subsample of heavily X-ray absorbed CSOs contains five sources, out of which three appeared to be suitable NuSTAR targets in terms of their expected X-ray fluxes above 10 keV: OQ+208, 2021+614, and 2MASX J15114125+0518089 (hereafter J1511+0518). OQ+208 was the first CSO ever observed and detected with NuSTAR, and its broadband X-ray spectroscopy was presented in Sobolewska et al. (2019b; hereafter S19b). A significant amount of X-ray absorbing column has been confirmed in this source as the result of the NuSTAR pointing, and it was inferred that the absorbing material could be associated with a toroidal, possibly patchy, obscurer. In this paper, we focus on 2021+614 and J1511+0518.

J1511+0518 ($z = 0.08418$) has an LS $\simeq 7.3$ pc (Polatidis & Conway 2003; Orienti & Dallacasa 2008) and a kinematic age of ~300 yr (An et al. 2012). It has been observed in X-rays with Chandra/ACIS-S for ~2 ks (Kuraszkiewicz et al. 2009). This short observation was revisited by Siemiginowska et al. (2016; hereafter S16) who reported on an unusually hard X-ray photon index, suggestive of a heavily absorbed X-ray continuum and/or a reflection-dominated X-ray spectrum (see also Trichas et al. 2013). S16 flagged J1511+0518 as a Compton thick (CT) candidate, namely a source with an intrinsic X-ray absorbing column density of $N_H > 1.5 \times 10^{24}$ cm^{-2}.

'2021+614 ($z = 0.227$) has an LS $\simeq 24.5$ pc and a kinematic age of ~400 yr (Tschager et al. 2000; Polatidis & Conway 2003). It has also been detected in X-rays in a ~5 ks Chandra/ACIS-S observation, and flagged as a CT candidate based on the properties of its 0.5–7 keV X-ray spectrum (S16). A deeper XMM-Newton observation of 2021+614 allowed S19b to determine that an obscuring matter with high intrinsic X-ray absorbing column is present in the source.

Here, we report on the NuSTAR observations of 2021+614 and J1511+0518, and on the XMM-Newton observation of J1511+0518. In addition, we analyze archival XMM-Newton/Chandra observations of the two sources. We model the broadband XMM-Newton and NuSTAR X-ray spectra of 2021+614 and J1511+0518 to uncover radiative processes that give rise to the X-ray emission of the targets. In this way, we constrain the properties of the environment in which these compact radio sources expand, the properties of their intrinsic hard X-ray emission, and we study their X-ray variability on timescales of years and decades.

Section 2 summarizes the details of the new and archival X-ray observations of the two CSOs, and outlines the data reduction procedure. In Section 3, we introduce the spectral models applied to characterize the X-ray emission of the sources. We present the main results of our analysis in Section 4 and discuss them further in Section 5. We present our conclusions and final remarks in Section 6. Throughout the paper, we assume a flat ΛCDM cosmology with $H_0 = 70$ km Mpc^{-1} s^{-1}, and $\Omega_\lambda = 0.73$, corresponding to the luminosity distances and conversion scales $d_L \simeq 1.14$ Gpc and 3.7 kpc arcsec^{-1} for 2021+614, and $d_L \simeq 384$ Mpc and 1.6 kpc arcsec^{-1} for J1511+0518.

2. Observations

The NuSTAR (Harrison et al. 2013) observations of 2021+614 and J1511+0518 were performed on 2018 July 7 for approximately 62 ks (ID 60401023002) and on 2019 January 8 for approximately 70 ks (ID 60401024002), respectively, using two telescopes, Focal Plane Module A (FPMA) and Focal Plane Module B (FPMB). In addition, J1511+0518 was observed for approximately 23 ks with XMM-Newton (ID 0822350101) on 2018 August 15. The details of these new observations, along with the archival XMM-Newton data for 2021+614 and Chandra data for both targets, including the resulting exposures and the net count rates for each instrument, are summarized in Table 1.

We used HEAsoft 6.29b and NuSTARDAS v2.1.1 software with the CALDB version 20210210 to process the NuSTAR data of both targets. We ran nupipeline and nuproducts to apply dead time correction, to account for South Atlantic Anomaly passages with SAAMODE = optimize and TENTACLE = yes, to apply new calibration, to extract spectra, and to generate appropriate response files. Both sources were clearly detected with NuSTAR (Figure 1). For the source spectra, we assumed a circle with the default radius of 20 pixels ($=49.''2$ for a pixel size of $2.''46$) centered on target positions (Table 1). For the background, we used annular regions with the same central coordinates, and with the default inner and outer radii of 50 and 80 pixels, respectively. The NuSTAR source and background extraction regions for 2021+614 and J1511+0518 are illustrated in Figures 1(a) and (c), respectively.

We used the standard XMM-Newton pipeline products for J1511+0518 (Processing Pipeline Subsystem event lists processed with Science Analysis Subsystem v.16.0). The resulting clean exposure times for each source are listed in Table 1. We note that the high background rates impacted approximately 50% of the originally scheduled exposures of J1511+0518. The XMM-Newton source and background extraction regions for J1511+0518 are shown in Figure 1(b).

Archival X-ray data exist for these CSOs (Table 1). Both of them have been observed with Chandra between 2003 and 2012 (Kuraszkiewicz et al. 2009; S16). Additionally, 2021+614 was observed with XMM-Newton in 2016 (S19a). We

Table 1
Summary of New and Archival X-Ray Observations

#	Source	R.A.	Decl.	Date	ID	Instrument	Exposure[a] (s)	Net Count Rate[b] ($\times 10^{-3}$ counts^{-1})	References
					New				
1	2021+614[c]	20 22 06.60	+61 36 51.60	2018-07-07	60401023002	FPMA	62177	7.6 ± 0.5	This work
						FPMB	60673	6.9 ± 0.5	This work
2	1511+0518	15 11 41.20	+05 18 09.22	2019-01-08	60401024002	FPMA	69980	4.7 ± 0.3	This work
						FPMB	69625	4.1 ± 0.4	This work
3	1511+0518	15 11 41.16	+05 18 10.70	2018-08-15	0822350101	PN	22676	45.1 ± 1.6	This work
						MOS1	20491	14.2 ± 0.9	This work
						MOS2	20444	12.0 ± 0.8	This work
					Archival				
4	2021+614	20 22 06.682	+61 36 58.79	2012-04-04	12853	ACIS-S	4784	11.2 ± 1.5	(1)
5	2021+614[c]	20 22 06.682	+61 36 58.79	2017-06-14	0784610301	PN	21624	34.1 ± 1.3	(2)
						MOS1	30214	10.3 ± 0.6	(2)
						MOS2	30214	11.4 ± 0.6	(2)
6	1511+0518	15 11 41.26	+05 18 09.27	2003-05-18	4047	ACIS-S	1994	24.5 ± 3.6	(3), (1)

Notes.
[a] Effective exposure after applying the standard filtering criteria.
[b] Net count rate recorded with FPMA/FPMB on board NuSTAR (3–40 and 3–20 keV energy band for 2021+614 and J1511+0518, respectively), PN/MOS1/MOS2 on board XMM-Newton (0.3–10 keV), and ACIS-S on board Chandra (0.5–7 keV).
[c] NuSTAR data are modeled jointly with the archival XMM-Newton data (S19b).
References. (1) Siemiginowska et al. (2016), (2) Sobolewska et al. (2019a), (3) Kuraszkiewicz et al. (2009).

use these archival observations to perform image analysis of J1511+0518 (Figure 1(d)), as well as to aid the broadband spectral modeling and to study the X-ray variability of both CSOs.

We used XSPEC v12.11.1 (Arnaud 1996) with W-statistic to model the X-ray spectra of 2021+614 and J1511+0518. For both sources, we performed simultaneous modeling of data sets from five instruments (NuSTAR's FPMA and FPMB; and XMM-Newton's European Photon Imaging Camera, EPIC PN, and Metal Oxide Semi-conductor, MOS1 and MOS2). Within XSPEC, we ran the Markov Chain Monte Carlo Metropolis–Hastings algorithm with the chain length of 10,000 and the burn-in parameter of 2000 to derive the 90% confidence errors on the model parameters, fluxes, and intrinsic luminosities.

3. Spectral Models

First, we quantified the NuSTAR and XMM-Newton spectra separately using a phenomenological model consisting of an absorbed power law. Both, the Galactic hydrogen column density along the line of sight, $N_{H,Gal}$ (Dickey & Lockman 1990), and the host galaxy hydrogen column density, $N_{H,z}$, have been taken into account. The model can be written as $M_0 = A \times M_{abs} \times$ powerlaw, where $A = [A_{MOS1}, A_{MOS2}, A_{FPMA}, A_{FPMB}]$ denotes a set of constants accounting for the instrumental cross-calibration relative to the PN instrument, and

$$M_{abs} = \exp\left(-N_{H,Gal}\sigma_E\right)\exp\left(-N_{H,z}\sigma_{E(1+z)}\right), \quad (1)$$

where σ_E is the photoelectric cross section (Verner et al. 1996). In XSPEC, $M_{abs} =$ phabs $\times$ zphabs.

Then, motivated by the broadband X-ray modeling of the CSO OQ+208 (S19b) and by the XMM-Newton modeling of 2021+614 (S19a), we explored a more complex model for a toroidal reprocessor, with the goal of describing the broadband X-ray continua of 2021+614 and J1511+0518. The model of our choice, borus02 (Baloković et al. 2018), assumes that the reprocessing medium is a sphere of cold and neutral gas with conical cutouts at both poles, approximating a torus. It provides the flexibility to fit for the torus covering factor, $CF_{tor} = \cos(\theta_{tor})$, where θ_{tor} is the half-opening angle of the polar cutouts that is allowed to vary in the range 0°–84° in the model. We note that CF_{tor} is fixed to 0.5 in another commonly used toroidal reprocessor model, mytorus (Yaqoob 2012). The full model was defined as

$$M = A \times M_{abs} \times [M_{abs,los} \times \text{cutoffpl} + \text{borus02} + C_{pl} \times \text{cutoffpl}]. \quad (2)$$

It included the following components: the Galactic and host galaxy intrinsic absorption, M_{abs}; the line-of-sight absorption at the redshift of the source acting on the intrinsic continuum including Compton scattering losses out of the line of sight,

$$M_{abs,los} = \exp(-N_{H,los}\sigma_{E(1+z)})\exp(-N_{H,los}\sigma_T), \quad (3)$$

where σ_T is the Thomson cross section, and $M_{abs,los} =$ zphabs $\times$ cabs in XSPEC; the torus reprocessing, borus02; and the scattered (not absorbed) component, $C_{pl} \times$ cutoffpl, with C_{pl} denoting its relative normalization with respect to the incident power law (see Baloković et al. 2018). We chose the cutoffpl model to characterize the intrinsic continuum because it provides the flexibility to quantify any high-energy cutoff possibly present in the NuSTAR data. We applied the relevant reflected and line emission table model provided by Baloković et al. (2018), with Fe abundance fixed to the solar abundance, to express the torus reprocessed component. Note that the Fe emission in the 6–7 keV (rest-frame) region is computed self-consistently within the framework of the borus02 model. The inclination angle, θ_{inc}, was fixed to 80° because the CSOs are believed to be viewed edge on, through the obscuring torus, given the
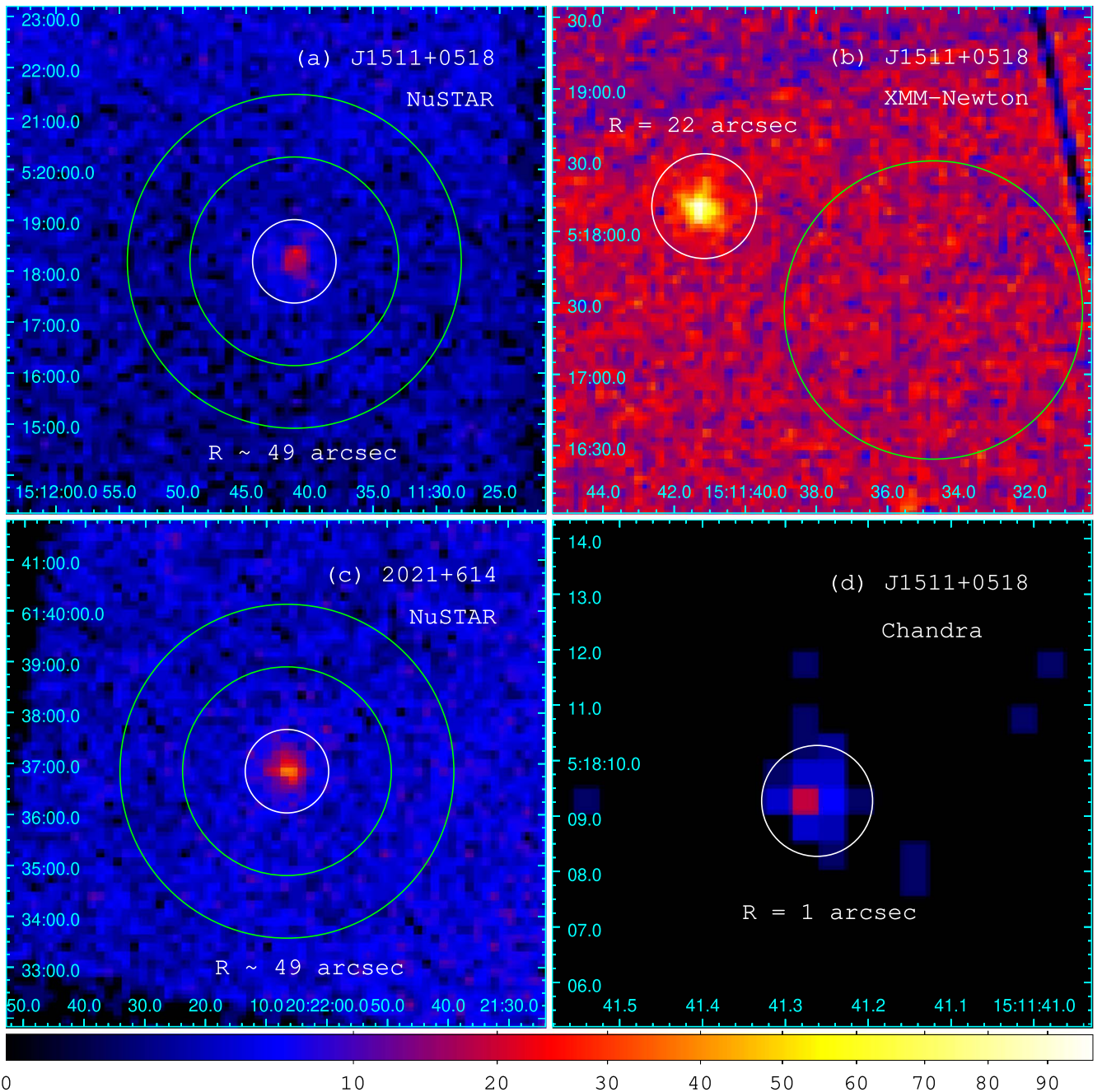
Figure 1. Images of the two CSOs showing the detections, and the source (white, with radius R) and background (green) extraction regions. (a) The 3–20 keV NuSTAR FPMA image of J1511+0518 binned by 4 pixels; $R = 20$ px $\simeq 49''$. (b) The 0.3–10 keV XMM-Newton EPIC PN image of J1511+0518 binned by 64 pixels. (c) The 3–40 keV NuSTAR FPMA image of 2021+614 binned by 4 pixels; $R = 20$ px $\simeq 49''$. (d) The archival 0.5–7 keV Chandra ACIS-S image of J1511 +0518. Extended X-ray emission surrounding J1511+0518 on scales $>1'' \simeq 1.6$ kpc at the redshift of the source can be seen. The square root scale color bar is common to all panels.

symmetric nature of their radio structures and the underlying assumption that the jet axis is perpendicular to the plane of the torus. We checked, however, that our data are not sensitive to this parameter, which is allowed to vary in the range 19°–87° in the model.

4. Results

The phenomenological model provided important insights into the X-ray properties of our two CSOs, which could be quantified and interpreted in the framework of a model incorporating a toroidal reprocessor. The applied torus model

was found to fit well the broadband X-ray data for both 2021 +614 and J1511+0518 confirming that their compact jets evolve within dense circumnuclear environments with $N_{\rm H,tor} \gtrsim 10^{23}$ cm^{-2}. In J1511+0518, an additional soft X-ray component, subject to both Galactic, $N_{\rm H,Gal}$, and host galaxy, $N_{\rm H,z}$, column densities, was added to alleviate the residuals seen in the ratio of data to model below 1 keV, likely due to highly ionized O and Ne/Fe. This finding was corroborated by the archival Chandra image of J1511+0518, which revealed that this CSO may be embedded within the extended, galactic-scale X-ray halo. We note that no evidence for extended X-ray emission in 2021+614 has been found in the analysis by S16.

Table 2
Designations and Properties of Spectral Models with a Toroidal Reprocessor

	Thermal Plasma	$N_{\mathrm{H,tor}} = N_{\mathrm{H,los}}$
Model A	no	yes
Model B	no	no
Model C	yes	yes
Model D	yes	no

The line-of-sight absorbing column density, $N_{\mathrm{H,los}}$, a parameter of $M_{\mathrm{abs,los}}$, was tied to the absorbing column density of the torus, $N_{\mathrm{H,tor}}$. However, we also investigated the quality of fits with $N_{\mathrm{H,tor}}$ and $N_{\mathrm{H,los}}$ independent of each other, and we discuss them in Section 5.2. We summarize the designations and properties of the best-fitting models with a toroidal reprocessor in Table 2.

The FPMA and FPMB normalization constants relative to PN, A_{FPMA} and A_{FPMB}, suggest that in 2021+614 the normalization of the incident X-ray power law is variable on the timescale of years. This type of variability has been tentatively detected also in J1511+0518 when comparing the XMM-Newton and NuSTAR data. The joint fit did not provide evidence for any photon index variability between the XMM-Newton and NuSTAR observations in either source. We did not detect any high-energy cutoff in the X-ray spectra of the sources, and therefore we fixed the cutoff energy at 300 keV in all the fits. The data and best-fitting models are presented in Figure 2, and the model parameters are listed in Table 3, cols. (4)–(6). Our detailed results are described and discussed in the following sections.

4.1. 2021+614

We detected 2021+614 with NuSTAR FPMA (FPMB) up to 40 keV with a high signal-to-noise ratio (S/N), S/N ≃ 17 (15) in the 3–40 keV energy band. The S/N was high, S/N ≃ 12 (11), in both the soft, 3–10 keV, and hard, 10–40 keV, energy bands. This is the first detection of this CSO at energies >10 keV (Figure 1(c)).

The phenomenological absorbed power-law model applied to the NuSTAR data resulted in an intrinsic absorbing column consistent with zero, an unusually hard power-law index, $\Gamma \simeq 0.6$, and with the residuals suggesting the presence of the 6.4 keV Fe emission line and a reflection hump in the spectrum. Thus, the properties of the NuSTAR spectrum appeared to echo those of the XMM-Newton X-ray spectrum presented in S19a.

Indeed, the model of a toroidal absorber constructed as in the S19a analysis, applied simultaneously to the archival XMM-Newton and new NuSTAR data, resulted in a good quality fit, presented in Figure 2(a). The fit parameters are listed in Table 3, col. (4). The deabsorbed 2–10 keV rest-frame luminosity of the incident hard X-ray power law was found to be of the order of 10^{44} erg s^{-1}. We constrained the half-opening angle of the reprocessor to the range $\theta_{\mathrm{tor}} = 28°–72°$. We found that approximately 13% of the direct power law is scattered into the line of sight without suffering from absorption. The best-fit model resulted in a relatively hard photon index, $\Gamma = 1.45^{+0.09}_{-0.05}$, consistent at 90% confidence level with the lower end of the photon indices tabulated within the `borus02` model, $\Gamma_{\mathrm{b02}} = 1.4$–2.6. The cross-normalization constants, A_{FPMA} and A_{FPMB}, relative to PN, strongly suggest X-ray variability of the direct power-law flux in 2021+614 on the timescale of years.
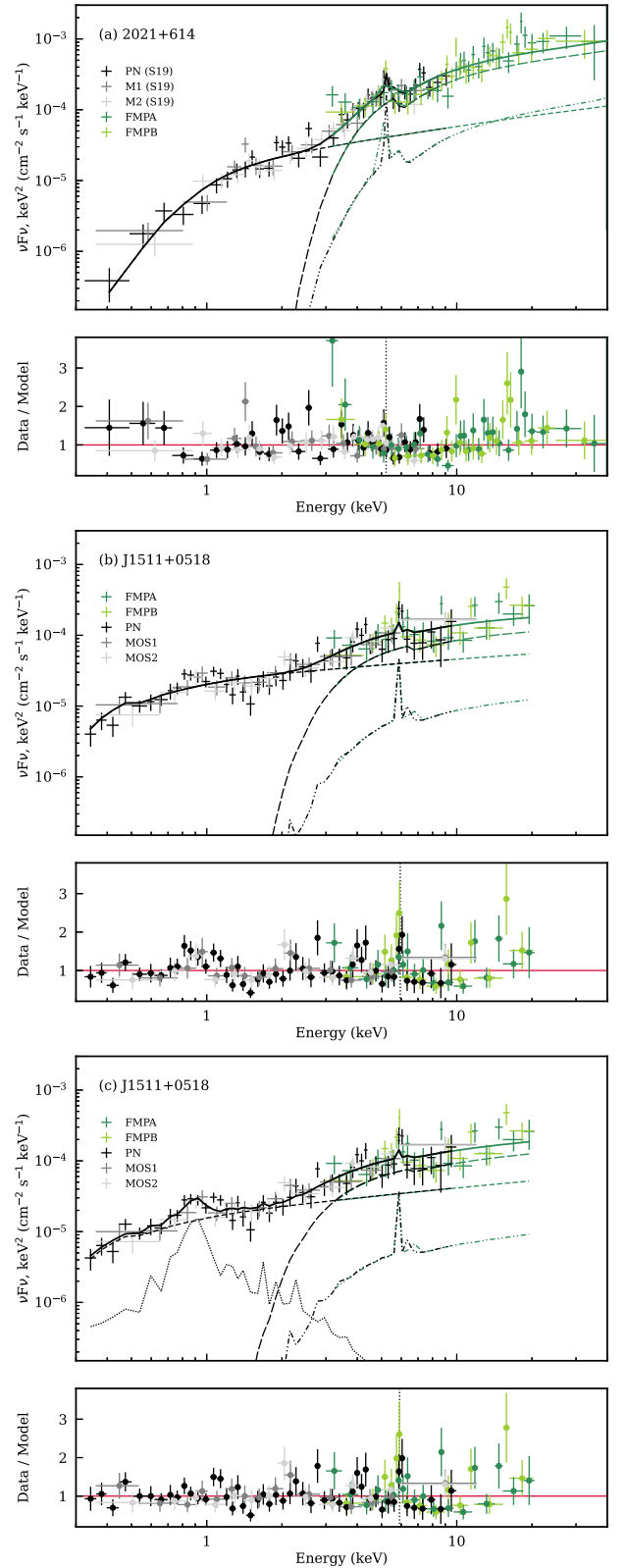

Figure 2. Best-fit *unfolded* models (solid), data (crosses), model components, and data–model ratios. (a) 2021+614. (b) J1511+0518 without the thermal plasma component. (c) J1511+0518 with the thermal plasma component. Vertical lines mark the rest-frame energy of the fluorescent Fe Kα emission line. The model components are as follows: direct continuum with intrinsic line-of-sight absorption (long-dashed), scattered continuum (short-dashed), reflection from a torus including the Fe Kα line (dot–short-dashed), thermal plasma (dotted). The NuSTAR data are binned, for presentation purposes only, so that each bin has a 3σ detection limit.

Table 3
Parameters of the Best-fitting Spectral Models

Parameter Description	Symbol	Unit	2021+614	J1511+0518	
			Model A	Model A	Model C
(1)	(2)	(3)	(4)	(5)	(6)
Redshift	z		0.227	0.08418	0.08418
Galactic absorbing column	$N_{\mathrm{H,Gal}}$	$10^{20}\,\mathrm{cm}^{-2}$	14.01	3.29	3.29
Host galaxy intrinsic absorbing column	$N_{\mathrm{H,z}}$	$10^{21}\,\mathrm{cm}^{-2}$	$2.4^{+1.3}_{-1.0}$	$0.43^{+0.31}_{-0.12}$	$0.3^{+0.3}_{-0.2}$
Apec temperature	kT	keV	...	...	$1.04^{+0.10}_{-0.17}$
Photon index	Γ		$1.45^{+0.09}_{-0.05}$	$1.70^{+0.15}_{-0.05}$	$1.62^{+0.11}_{-0.09}$
Torus half-opening angle	θ_{tor}	deg	49^{+23}_{-21}	<32	<47
Torus column density	$N_{\mathrm{H,tor}}$	$10^{23}\,\mathrm{cm}^{-2}$	$3.7^{+0.8}_{-0.5}$	$1.3^{+0.6}_{-0.4}$	$0.9^{+0.3}_{-0.2}$
Line-of-sight column density	$N_{\mathrm{H,los}}$	$10^{23}\,\mathrm{cm}^{-2}$	$N_{\mathrm{H,tor}}$	$N_{\mathrm{H,tor}}$	$N_{\mathrm{H,tor}}$
Scattered power-law relative norm	C_{pl}		$0.13^{+0.05}_{-0.02}$	$0.43^{+0.06}_{-0.10}$	$0.38^{+0.11}_{-0.08}$
Cross-calibration constants relative to PN					
MOS1	A_{MOS1}		$0.99^{+0.14}_{-0.08}$	$1.09^{+0.11}_{-0.17}$	$1.09^{+0.16}_{-0.09}$
MOS2	A_{MOS2}		$1.06^{+0.12}_{-0.11}$	$0.95^{+0.13}_{-0.11}$	$0.95^{+0.08}_{-0.14}$
FPMA	A_{FPMA}		$0.59^{+0.10}_{-0.08}$	$0.97^{+0.27}_{-0.12}$	$0.97^{+0.16}_{-0.09}$
FPMB	A_{FPMB}		$0.57^{+0.07}_{-0.08}$	$0.89^{+0.12}_{-0.07}$	$0.89^{+0.09}_{-0.08}$
Line equivalent width[a]	EW	eV	~213	~97	~77
2–10 keV					
Observed absorbed flux[b]	$F_{2-10\,(\mathrm{oa})}$	$10^{-13}\,\mathrm{erg\,s^{-1}\,cm^{-2}}$	$3.67^{+0.10}_{-0.43}$	$2.15^{+0.05}_{-0.18}$	$2.17^{+0.14}_{-0.26}$
Rest-frame absorbed luminosity[c]	$L_{2-10\,(\mathrm{ra})}$	$10^{43}\,\mathrm{erg\,s^{-1}}$	$4.11^{+0.11}_{-0.48}$	$0.35^{+0.07}_{-0.03}$	$0.36^{+0.02}_{-0.04}$
Rest-frame deabsorbed luminosity[d]	$L_{2-10\,(\mathrm{rd})}$	$10^{43}\,\mathrm{erg\,s^{-1}}$	~11	~0.38	~0.37
0.3–20 keV					
Observed absorbed flux[b]	$F_{0.3-20\,(\mathrm{oa})}$	$10^{-13}\,\mathrm{erg\,s^{-1}\,cm^{-2}}$	$9.6^{+0.5}_{-1.4}$	$4.4^{+0.2}_{-0.6}$	$4.50^{+0.14}_{-0.26}$
Rest-frame absorbed luminosity[c]	$L_{0.3-20\,(\mathrm{ra})}$	$10^{43}\,\mathrm{erg\,s^{-1}}$	$11.7^{+0.4}_{-1.7}$	$0.74^{+0.03}_{-0.09}$	$0.75^{+0.05}_{-0.10}$
Rest-frame deabsorbed luminosity[d]	$L_{0.3-20\,(\mathrm{rd})}$	$10^{43}\,\mathrm{erg\,s^{-1}}$	~25	~0.88	~0.82
20–40 keV					
Observed absorbed flux[b]	$F_{20-40\,(\mathrm{oa})}$	$10^{-13}\,\mathrm{erg\,s^{-1}\,cm^{-2}}$	$8.8^{+0.7}_{-1.5}$	$2.2^{+0.3}_{-0.7}$	$2.4^{+0.4}_{-0.5}$
Rest-frame absorbed luminosity[c]	$L_{20-40\,(\mathrm{ra})}$	$10^{43}\,\mathrm{erg\,s^{-1}}$	$12.1^{+1.1}_{-2.1}$	$0.37^{+0.05}_{-0.11}$	$0.40^{+0.07}_{-0.09}$
Rest-frame deabsorbed luminosity[d]	$L_{20-40\,(\mathrm{rd})}$	$10^{43}\,\mathrm{erg\,s^{-1}}$	~12	~0.26	~0.29
Fit statistics[e]	W statistic		2020.06	1090.46	1066.36
Degrees of freedom	d.o.f.		1920	945	943

Notes. Errors represent 90% confidence intervals. The cutoff energy was fixed to 300 keV in all models. Fluxes, luminosities, and equivalent widths computed based on the models fitting the PN data sets.
[a] Equivalent width of the fluorescent 6.4 keV Fe $K\alpha$ emission line computed with respect to the total continuum. The line was computed self-consistently with the `borus02` model.
[b] Total flux in the energy band corresponding to the observed frame energies, not corrected for absorption.
[c] Total luminosity in the energy band corresponding to the rest-frame energies, not corrected for absorption.
[d] Luminosity of the direct power-law component in the energy band corresponding to the rest-frame energies, corrected for absorption.
[e] https://heasarc.gsfc.nasa.gov/xanadu/xspec/manual/XspecManual.html.

4.2. J1511+0518

J1511+0518 was detected with both NuSTAR and XMM-Newton (see Figures 1(a) and (b), respectively). We detected J1511+0518 with NuSTAR FPMA (FPMB) up to 20 keV with a high S/N = 14 (12) in the 3–20 keV energy band, with S/N = 12 (10) in the 3–10 keV band, and with S/N = 7 (6.5) in the 10–20 keV band. This is the first detection of this CSO at energies >10 keV.

The phenomenological model applied to the XMM-Newton data resulted in the intrinsic absorbing column consistent with zero and a rather hard photon index, $\Gamma \simeq 1.25$, both consistent at the $2\sigma-3\sigma$ confidence level with the results of S16 based on the analysis of the archival Chandra data. However, the XMM-Newton model residuals showed a complex curvature indicating that additional spectral components, including the fluorescent 6.4 keV Fe emission line, are required to obtain a good quality fit. The phenomenological model applied to the NuSTAR data also showed residuals supporting the presence of the 6.4 keV Fe emission in the spectrum of J1511+0518. By including the `zgauss` component with line energy fixed to 6.4 keV and line width σ fixed to 0.01 keV, we found the line equivalent widths with respect to the total continuum of EW ~ 480 and ~710 eV in the XMM-Newton and NuSTAR spectra, respectively. We obtained $\Gamma = 1.3^{+0.5}_{-0.2}$ for the NuSTAR spectrum, consistent with the photon index derived from modeling the XMM-Newton data only.

We proceeded with the application of the toroidal reprocessor model to the NuSTAR and XMM-Newton data of J1511+0518. We obtained a relatively good quality fit with model

parameters as listed in Table 3, col. (5). However, we noticed a cluster of residuals in the 0.8–1 keV energy band in the data–model ratio (Figure 2(b)). We explored the possibility that an extra spectral component contributes to the soft X-ray spectrum of this CSO. We analyzed the archival 2 ks Chandra image and discovered that J1511+0518 is most likely embedded in an extended X-ray halo (Figure 1(d)). The number of counts detected from the source with Chandra in this short ∼2 ks observation, ∼50 cts, was not sufficient to perform a spatially resolved spectroscopy. However, we tested for the extended X-ray emission by including in the model a hot, collisionally ionized plasma component, apec, with solar abundance. We found that for $kT \simeq 1$ keV the $\lesssim 1$ keV residuals became less significant, and the fit statistic decreased by $\Delta \simeq 24$ (Table 3, col. (6); Figure 2(c)). The models with and without the thermal component resulted in parameters, which are consistent with each other at 90% confidence level.

Our results imply that the nuclear X-ray emission of J1511+0518 is seen through an obscuring torus with an intrinsic absorbing column $N_{\mathrm{H,tor}} \gtrsim 10^{23}$ cm^{-2}, and a host galaxy intrinsic absorber with $N_{\mathrm{H,z}} \simeq 10^{20}$ cm^{-2}. The deabsorbed 2–10 keV rest-frame luminosity of J1511+0518 was found to be of the order of 4×10^{42} erg s^{-1}. We obtained a photon index in the range $\Gamma \sim 1.6$–1.7. We estimated only an upper limit to the half-opening angle of the reprocessor, $\theta_{\mathrm{tor}} \lesssim 32°$–47°, consistent with a sphere (i.e., $\theta_{\mathrm{tor}} = 0°$) at 90% confidence level. However, the relatively high fraction of the scattered direct power law in the best-fitting model, 38%–43%, suggests a half-opening angle larger than zero, or a reprocessor with a porous structure (see the discussion of the $N_{\mathrm{H,los}} \neq N_{\mathrm{H,tor}}$ case in Section 5). The cross-normalization constants are consistent with each other and do not provide strong evidence for X-ray variability between the XMM-Newton and NuSTAR data sets.

5. Discussion

We observed with NuSTAR two CT CSO candidates identified in S16, namely 2021+614 and J1511+0518. In addition, we observed J1511+0518 with XMM-Newton. 2021+614 and J1511+0518 were detected with NuSTAR up to 40 and 20 keV, accordingly. As the result of our observations, we increased the sample of hard (>10 keV) X-ray detected CSOs from one (OQ+208 discussed previously in S19b) up to three. We modeled the broadband XMM-Newton/NuSTAR X-ray spectra of our sources with a toroidal reprocessor model defined with Equation (2), with an additional thermal plasma component in J1511+0518. Implications of our modeling are discussed in this section.

5.1. Extended X-Ray Emission in J1511+0518

X-ray emission extended on the scale of the host galaxies has been reported previously in two of the closest and most compact CSOs, PKS 1718-649 ($z = 0.0144$, LS $\simeq 2$ pc, intermediate spiral host galaxy; S16; Beuchert et al. 2018) and NGC 3894 ($z = 0.01075$, LS $\simeq 4$ pc, elliptical host galaxy; Balasubramaniam et al. 2021). In both cases, it was found to be compatible with a hot, collisionally ionized medium, with the temperature of $kT \sim 0.8$ keV. Beuchert et al. (2018) argued that the properties of the extended emission in PKS 1718-649 are consistent with being due to supernovae in the host galaxy.

We analyzed the archival Chandra image of J1511+0518 and found evidence for the X-ray emission extending beyond the $1''$ ($\simeq 1.6$ kpc at the redshift of the source) circular extraction region centered at the position of the source. The Sloan Digital Sky Survey image shows that the host of J1511+0518 is a red elliptical galaxy (Kosmaczewski et al. 2020), and so it is expected to be embedded in a hot X-ray halo. Our spectral fit with a collisionally ionized plasma model resulted in the plasma temperature of $kT = 1.04^{+0.10}_{-0.18}$ keV, comparable with the temperatures measured for PKS 1718-649 and NGC 3894, as well as for hot X-ray halos in various galaxy samples (e.g., O'Sullivan et al. 2003; Goulding et al. 2016).

The projected parsec-scale size of the radio structures in J1511+0518 suggests that the feedback of the central radio source may be excluded as the origin of the extended X-ray emission in this CSO. However, it is worth noting that Atacama Large Millimeter/submillimeter Array observations of several CSOs show molecular outflows on scales much larger than those from the currently detected radio jets (CSO PKS 1718+649, Papachristou et al. 2021; see also Aalto et al. 2016; Fernández-Ontiveros et al. 2020). Moreover, Zovaro et al. (2019) argued that in CSO 4C31.04 the apparent discrepancy between the extent of the gas shocked by a jet-blown bubble and the ∼100 pc scale radio jet can be explained with hydrodynamical simulations in which the brightest regions of the synchrotron emitting plasma are temporarily halted by dense clumps, while less bright plasma can expand freely through the porous ISM (see also in this context Wagner et al. 2012; Mukherjee et al. 2018). A deeper Chandra image of J1511+0518 is needed to perform a more in-depth spatially resolved spectroscopy of its X-ray halo.

5.2. Nuclear Intrinsic Absorption

We confirmed the presence of a significant intrinsic X-ray absorbing column density of nuclear origin in 2021+614, and measured it in J1511+0518. In neither source did we find obscuring matter with a column density in the CT regime when the line-of-sight and torus column densities are tied to each other, $N_{\mathrm{H,los}} = N_{\mathrm{H,tor}}$. Nevertheless, at $N_{\mathrm{H,tor}} \simeq (0.9$–$4.0) \times 10^{23}$ cm^{-2}, the measured intrinsic absorbing column densities support the conclusion that these two radio jets expand in dense environments, as long as the gas that is responsible for the X-ray absorption is distributed on scales comparable with the scales of the radio structures (i.e., the central ∼7–25 pc). However, if the high column X-ray absorbing gas is concentrated very close to the nucleus, the surrounding environment may be of low density, and the radio jets may expand freely. Interestingly, the N_{H} (X-rays)–N H I (radio) correlation found in Ostorero et al. (2017) suggests that the gas responsible for the X-ray obscuration and the H I responsible for the radio absorption may be part of the same, unsettled gaseous structure that extends over 100 parsec scales.

For completeness, we explored the case with $N_{\mathrm{H,los}} \neq N_{\mathrm{H,tor}}$, which could be interpreted in terms of a reprocessor with a porous structure. We found $N_{\mathrm{H,tor}} = 1.9^{+2.0}_{-0.6} \times 10^{24}$ cm^{-2}, and $N_{\mathrm{H,los}} = 3.05^{+0.40}_{-0.11} \times 10^{23}$ cm^{-2} for 2021+614 (model (B)), and $N_{\mathrm{H,tor}} = 6^{+8}_{-4} \times 10^{23}$ cm^{-2}, and $N_{\mathrm{H,los}} = 0.7^{+0.4}_{-1.1} \times 10^{23}$ cm^{-2} for J1511+0518 (model (D); see Table 2 for definition of models (B) and (D)). It can be seen that the torus and line-of-sight column densities are not consistent with each other in these models at 90% confidence level, while the remaining parameters are in excellent agreement with those presented in Table 3 for the $N_{\mathrm{H,los}} = N_{\mathrm{H,tor}}$ case (i.e., model (A) for 2021+614 and model (C) for J1511+0518). However, with a relatively minor drop in the
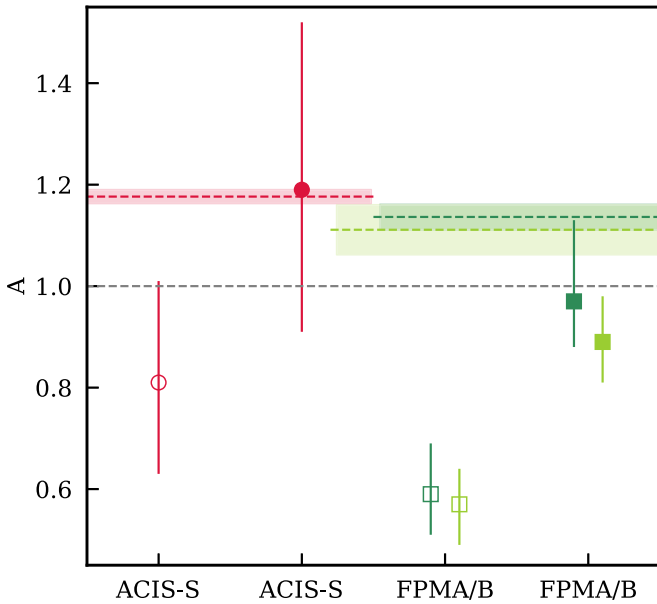
Figure 3. The normalization of the incident power law recorded by ACIS-S and FPMA/B relative to that of XMM-Newton/PN. Error bars represent 90% confidence level. Shaded regions represent cross-calibration results of Madsen et al. (2017). Open symbols, 2021+614 (model (A)); filled symbols, J1511 +0518 (model (C)). Red circles, Chandra/ACIS-S; dark green squares, NuSTAR/FPMA; light green squares, NuSTAR/FMPB. Red horizontal line, expected ACIS-S level; and dark and/or light green horizontal lines and shaded regions, expected FPMA/B levels, in the case of no flux variability compared with XMM-Newton/PN (gray horizontal line).

fit statistic of $\Delta \simeq 20$ and $\Delta \simeq 6$ in 2021+614 and J1511+0518, respectively, for one extra parameter, the data provide only a tentative evidence for a porous structure of the reprocessor, and intrinsic column densities reaching the CT regime. We note that a similar conclusion was reached for the CSO OQ+208, where the torus column density was consistent with the CT regime in the case of $N_{H,los} \neq N_{H,tor}$, with only a minor decrease of the overall fit statistic compared to the case when the two column densities were tied to each other (S19b).

5.3. X-Ray Variability

X-ray variability has been previously reported in CSO PKS 1718-649 (Beuchert et al. 2018) and OQ+208 (S19b). In the case of PKS 1718-649, the analysis of three Chandra and one XMM-Newton exposures revealed variability on the timescale of years in both the source intrinsic column density, $N_{H,z} = (0.3-0.7) \times 10^{22}$ cm^{-2}, and the 0.5–10 keV flux of the incident hard X-ray power law, $(5.4-11.6) \times 10^{-13}$ erg cm^{-2} s^{-1}. In the case of OQ+208, the modeling of one Chandra, one XMM-Newton, and one NuSTAR exposures revealed that the flux of the incident hard X-ray power law increased by up to 50% on the timescale of years.

Existing multiepoch data of the two CSOs discussed in this paper are not suitable to study the variability of the intrinsic column density because of the lack of the softest X-ray band coverage in the NuSTAR spectra and insufficient spectral constraints provided when fitting individually the archival Chandra observations, leaving only one soft X-ray band XMM-Newton data set per source. However, in the following, we discuss the variability of the photon index and of the flux of the direct hard X-ray continuum. Inferring flux variability from observations performed with various observatories is difficult

due to the cross-calibration uncertainties. Here, we refer to the cross-calibration constants reported by Madsen et al. (2017) from simultaneous observations with X-ray telescopes including XMM-Newton, NuSTAR, and Chandra, of active galaxies 3C 273 and PKS 2155-304: PN/ACIS-S = 0.85 ± 0.01, PN/ FPMA = 0.88 ± 0.02, and PN/FPMB = 0.90 ± 0.04.[6] We estimate A_{ACIS-S} by including the archival Chandra data in the joint best-fit model, with the aim to increase the baseline of our X-ray variability study. Note that in Figure 3 we plot the observed and expected cross-normalization constraints relative to PN (i.e., the inverse of the Madsen et al. 2017 cross-calibration constants).

5.3.1. 2021+614

In 2021+614, the spectral parameters obtained from a joint XMM-Newton and NuSTAR modeling are in agreement with the parameters obtained by modeling the XMM-Newton data alone, except for the photon index, which is harder at 90% confidence level in the joint fit of the XMM-Newton and NuSTAR data ($\Gamma = 1.45^{+0.06}_{-0.05}$) than in the fit of the XMM-Newton data alone ($\Gamma = 1.7^{+0.2}_{-0.1}$; S19a). It is possible that the photon index varied on timescales of years between the XMM-Newton and NuSTAR observations, and NuSTAR data above 10 keV dominate the estimate of the photon index in the joint fit. However, given that the spectral coverage of the XMM-Newton data is limited to <10 keV, we argue in favor of a scenario in which the joint fit utilizing broadband data enabled improved constraints on the shape of the underlying continuum in this high N_H source, rather than the scenario in which the photon index varied.

Nevertheless, we found that in 2021+614 the $A_{FPMA(B)}$ normalization constants deviate significantly from the expected ones (Figure 3). Additionally, we estimated the normalization constant of the archival Chandra spectrum relative to that of XMM-Newton/PN, $A_{ACIS-S} = 0.81^{+0.20}_{-0.19}$, which is also below the level expected in case of no flux variability compared with the XMM-Newton/PN observation. All in all, we conclude that the normalization, and thus the flux of the incident X-ray power law in 2021+614 could increase by ~50% between the 2012 Chandra and 2017 XMM-Newton observations, and decrease by ~50% between the 2017 XMM-Newton and the 2018 NuSTAR observations.

5.3.2. J1511+0518

We estimated the normalization constant of the archival Chandra spectrum relative to that of XMM-Newton/PN, $A_{ACIS-S} = 1.2^{+0.3}_{-0.3}$, and concluded that it is in agreement with that expected based on cross-calibration studies (Figure 3). We found that the $A_{FPMA/(B)}$ normalization constants are consistent with each other, but the A_{FPMB} constant is inconsistent with the cross-calibration constants reported by Madsen et al. (2017). We thus report a tentative decrease in the flux of J1511 +0518 by ~20% between the 2018 XMM-Newton and the 2019 NuSTAR observations.

---

[6] We note that Marshall et al. (2021) show an agreement, within the uncertainties, between various emission line fluxes measured from supernova remnant SNR 1E0102 with Chandra/ACIS-S3 and XMM-Newton/PN; however, no comparison with NuSTAR is presented by these authors.

5.4. Broadband X-Ray Properties of the Nucleus

The nuclear X-ray continua of both NuSTAR observed CSOs could be described well by a model of a toroidal reprocessor (Baloković et al. 2018). Consistent with high intrinsic column density (Section 5.2), the continua were found to be dominated by the scattered power-law component below $\sim$3 keV, and by the direct power law above $\sim$3 keV.

Our first ever detection of the fluorescent 6.4 keV Fe emission line in J1511+0518, included self-consistently in the reprocessed continuum, confirms the expectations following from the radio morphology that the X-ray spectrum of J1511+0518 is not dominated by a beamed emission. In addition to 2021+614 (S19a) and J1511+0518, the Fe line fluorescence consistent with Kα has been reported previously in the X-ray spectra of two other CSOs, OQ+208 (Guainazzi et al. 2004; S19b) and NGC 3894 (Balasubramaniam et al. 2021). All four sources are extremely compact in the radio band (LS $\simeq$ 4–16 pc). However, they show a range of intrinsic column densities, $\sim 10^{22}$–10^{24} cm^{-2}, and only NGC 3894 has been detected in the γ-ray band with Fermi/Large Area Telescope (Principe et al. 2020, 2021). Ionized Fe emission at energies >6.4 keV has also been reported in several CSOs (see a summary in Balasubramaniam et al. 2021).

The relative spectral contribution of the component reprocessed by the torus was higher in 2021+614 than that in J1511+0518, with the EW of the Fe Kα emission line with respect to the total continuum of $\sim$213 eV in 2021+614 and $\sim$77–97 eV in J1511+0518. The reflected and scattered components become comparable above 20–40 keV in 2021+614. The equivalent width of the fluorescent Fe Kα line resulting from the torus modeling of the J1511+0518 data was lower than that estimated from a simple absorbed power-law model fit to the XMM-Newton-only data (EW $\sim$ 480 eV) or the NuSTAR-only data (EW $\sim$ 710 eV), as it can be appreciated in the data–model residuals near the rest-frame energy $\sim$6.4 keV in Figures 2(b)–(c). This may indicate that the nuclear Fe Kα emission, accounted for by the torus model, is accompanied by a contribution from extended Fe Kα emitting regions, and/or contaminating off-nuclear point sources, similar to those resolved on tens to one hundred parsec scales in a few nearby galactic centers, including that of the Milky Way (e.g., Ponti et al. 2010; Marinucci et al. 2012, 2017; Arévalo et al. 2014; Fabbiano et al. 2018, 2019; see also a recent review by Fabbiano & Elvis 2022 and references therein). This scenario was discussed by S19b also in the case of CSO OQ+208. In J1511+0518 it seems to be supported by the apparent increase of the EW, measured relative to the continuum modeled by a power law, in the NuSTAR data compared to the EW measured from the higher spacial resolution XMM-Newton data. However, a possible power-law flux variability between the XMM-Newton and NuSTAR observations makes this assertion uncertain. Unfortunately, subkiloparsec scales are not resolvable in our CSOs with the current X-ray instrumentation. Alternative scenarios include deviations from the assumptions of the `borus02` model in terms of the geometry of the reflecting medium (e.g., Buchner et al. 2021) and/or the dynamics of the source of X-rays (e.g., a source of X-rays moving toward or away from the reflector instead of a stationary isotropic source, Beloborodov 1999), and/or Fe abundance, which deviates significantly from the assumed solar abundance.

The two CSOs host black holes with comparable masses, $M_{BH} \sim 4 \times 10^8\, M_\odot$ (J1511+0518, Wójtowicz et al. 2020) and $M_{BH} \sim 8 \times 10^8\, M_\odot$ (2021+614; Wu 2009); yet we found that their intrinsic X-ray luminosities differ by approximately 1.5 orders of magnitude. The deabsorbed 0.3–40 keV rest-frame luminosities estimated at $\sim 1 \times 10^{43}$ erg s^{-1} in J1511+0518 and $\sim 4 \times 10^{44}$ erg s^{-1} in 2021+614. We found that the best-fit photon indices in 2021+614 and J1511+0518 cover the range $\Gamma \sim 1.4$–1.7 (Table 3). Interestingly, Wójtowicz et al. (2020) estimated the Eddington ratios at $\lambda_{Edd} = L_{bol}/L_{Edd} \simeq 0.01$ in both CSOs, where the bolometric luminosities, L_{bol}, were measured from the [O III] 5007 Å luminosity in 2021+614 and from the SED fitting in J1511+0518 (Wu 2009; Trichas et al. 2013).

In the recent years, many authors have presented evidence in favor of AGN following spectral states similar to those known from the X-ray binary field (e.g., Körding et al. 2006; Sobolewska et al. 2011; Ruan et al. 2019; Fernández-Ontiveros & Muñoz-Darias 2021; Moravec et al. 2022). Thus, it is tempting to draw on phenomenology of accreting stellar mass black holes to interpret our spectral results. We infer that the two sources considered in this work, and CSOs in general, show properties that are typical for X-ray binaries in the low–hard spectral states, which feature steady radio jets and are found at the onset and at the end of an X-ray binary outburst (e.g., Remillard & McClintock 2006; Done et al. 2007; Dunn et al. 2010; Fender & Belloni 2012; Heil et al. 2015): (i) compact, newly formed, radio jets; (ii) relatively hard X-ray photon indices (S19a reported $\Gamma \simeq 1.1$–2 for the 17 CSOs in their sample for which the X-ray photon index could be constrained); (iii) Eddington ratios in the range $\lambda_{Edd} \simeq 0.009$–0.2 (Wójtowicz et al. 2020); (iv) X-ray flux variability on the timescale of years (Section 5.3), corresponding to a few seconds or a few tens of Hz when scaled down to a typical X-ray binary.[7] However, we note that Wójtowicz et al. (2020) proposed that various spectral states could be found within the CSO class based on the estimated CSO bolometric luminosities, Eddington ratios, and the jet kinetic powers.

Several physical processes are known to give rise to a power-law-like X-ray emission characterized by a photon index comparable to that estimated in 2021+614 and J1511+0518, and CSOs and accreting black holes in general (e.g., inverse-Compton processes in radio lobes inflated by the expanding jets, Stawarz et al. 2008; Ostorero et al. 2010; X-ray jet or its base, e.g., Markoff et al. 2001, 2005; X-ray corona visible directly or through reflection/scattering, Guainazzi et al. 2004; S16; thermal emission of the ISM heated by the expanding jet, O'Dea et al. 2006). Modeling a broadband radio to high-energy spectral energy distribution may be the key to uncovering the dominant processes that give rise to the X-ray emission in our sources. For example, in the CSO PKS 1718-649, a combination of the inverse-Compton processes in the radio lobes and a weak X-ray corona were shown to provide the best match with the data from the radio to the γ-ray band (Sobolewska et al. 2022).

---

[7] Variability timescales scale with the black hole mass; we assumed a $10^8\, M_\odot$ and $10\, M_\odot$ black hole in a CSO and in an X-ray binary, respectively.

6. Conclusions

We studied the X-ray properties of two CSOs, 2021+614 and J1511+0518, observed and detected with XMM-Newton and NuSTAR. Our main findings are as follows.

1. We reported, for the first time, on the detections of both CSOs with NuSTAR at energies >10 keV.

2. The XMM-Newton/NuSTAR spectra of both CSOs could be described satisfactorily with the model of a toroidal reprocessor (Baloković et al. 2018). The resulting photon indices are in the range $\Gamma \simeq 1.4$–1.7, and the deabsorbed 2–10 keV rest-frame luminosity was estimated at $\sim 10^{44}$ erg s^{-1} and $\sim 4 \times 10^{42}$ erg s^{-1} in 2021 +614 and J1511+0518, respectively.

3. We detected, for the first time, the 6.4 keV Fe emission line in J1511+0518, confirming that that beamed jet emission does not contribute significantly to the X-ray spectrum of this CSO. We speculate that excess Fe Kα emission, possibly required by the J1511+0518 data in addition to the nuclear line, might be associated with extended regions like those resolved in the last decade in several nearby galaxies and reviewed by Fabbiano & Elvis (2022).

4. In the case of J1511+0518, we argued that the joint XMM-Newton and NuSTAR spectral analysis and Chandra image analysis support the presence of the extended X-ray emission component in the source. This finding prompted us to include a hot, collisionally ionized plasma with $kT \simeq 1$ keV in the model.

5. We detected X-ray variability in 2021+614. The normalization of the best-fitting direct X-ray power law showed variability of $\sim 50\%$ on the timescale of years; it increased between the 2012 Chandra observation and the 2017 XMM-Newton observation, and decreased between the 2017 XMM-Newton observation and the 2018 NuSTAR observation.

6. We tentatively detected X-ray variability in J1511+0518. It is possible that the normalization of the best-fitting direct X-ray power law decreased by $\sim 20\%$ on the timescale of years, between the 2018 XMM-Newton observation and the 2019 NuSTAR observation.

7. We constrained the intrinsic equivalent hydrogen column densities in 2021+614 and J1511+0518, and confirmed that they are $\gtrsim 10^{23}$ cm^{-2}. This result strengthens the findings of S19a that a subpopulation of CSOs with high intrinsic absorption is separated from CSOs with low intrinsic column density in the linear radio size versus radio power plane, and adds improved measurements to the X-ray N_H versus radio $N_{H\,I}$ correlation of Ostorero et al. (2017).

ORCID iDs

Małgosia Sobolewska ⓘ https://orcid.org/0000-0002-6286-0159
Aneta Siemiginowska ⓘ https://orcid.org/0000-0002-0905-7375
Giulia Migliori ⓘ https://orcid.org/0000-0003-0216-8053
Luisa Ostorero ⓘ https://orcid.org/0000-0003-3983-5980
Łukasz Stawarz ⓘ https://orcid.org/0000-0001-8294-9479
Matteo Guainazzi ⓘ https://orcid.org/0000-0002-1094-3147

References

Aalto, S., Costagliola, F., Muller, S., et al. 2016, A&A, 590, A73
An, T., & Baan, W. A. 2012, ApJ, 760, 77
An, T., Wu, F., Yang, J., et al. 2012, ApJS, 198, 5
Arévalo, P., Bauer, F. E., Puccetti, S., et al. 2014, ApJ, 791, 81
Arnaud, K. A. 1996, in ASP Conf. Ser. 101, Astronomical Data Analysis Software and Systems, ed. G. H. Jacoby & J. Barnes (San Francisco, CA: ASP), 17
Balasubramaniam, K., Stawarz, Ł., Cheung, C. C., et al. 2021, ApJ, 922, 84
Baloković, M., Brightman, M., Harrison, F. A., et al. 2018, ApJ, 854, 42
Beloborodov, A. M. 1999, ApJL, 510, L123
Beuchert, T., Rodríguez-Ardila, A., Moss, V. A., et al. 2018, A&A, 612, L4
Bicknell, G. V., Dopita, M. A., & O'Dea, C. P. O. 1997, ApJ, 485, 112
Buchner, J., Brightman, M., Baloković, M., et al. 2021, A&A, 651, A58
Callingham, J. R., Ekers, R. D., Gaensler, B. M., et al. 2017, ApJ, 836, 174
Callingham, J. R., Gaensler, B. M., Ekers, R. D., et al. 2015, ApJ, 809, 168
Dickey, J. M., & Lockman, F. J. 1990, ARA&A, 28, 215
Done, C., Gierliński, M., & Kubota, A. 2007, A&ARv, 15, 1
Dunn, R. J. H., Fender, R. P., Körding, E. G., et al. 2010, MNRAS, 403, 61
Fabbiano, G., & Elvis, M. 2022, in Handbook of X-ray and Gamma-ray Astrophysics, ed. C. Bambi & A. Santangelo (Singapore: Springer), doi:10.1007/978-981-16-4544-0_111-1
Fabbiano, G., Paggi, A., Siemiginowska, A., et al. 2018, ApJL, 869, L36
Fabbiano, G., Siemiginowska, A., Paggi, A., et al. 2019, ApJ, 870, 69
Fender, R., & Belloni, T. 2012, Sci, 337, 540
Fernández-Ontiveros, J. A., Dasyra, K. M., Hatziminaoglou, E., et al. 2020, A&A, 633, A127
Fernández-Ontiveros, J. A., & Muñoz-Darias, T. 2021, MNRAS, 504, 5726
Goulding, A. D., Greene, J. E., Ma, C.-P., et al. 2016, ApJ, 826, 167
Guainazzi, M., Siemiginowska, A., Rodriguez-Pascual, P., et al. 2004, A&A, 421, 461
Harrison, F. A., Craig, W. W., Christensen, F. E., et al. 2013, ApJ, 770, 103
Heil, L. M., Uttley, P., & Klein-Wolt, M. 2015, MNRAS, 448, 3339
Kawakatu, N., Nagai, H., & Kino, M. 2008, ApJ, 687, 141
Körding, E. G., Jester, S., & Fender, R. 2006, MNRAS, 372, 1366
Kosmaczewski, E., Stawarz, Ł., Siemiginowska, A., et al. 2020, ApJ, 897, 164
Kunert-Bajraszewska, M., Gawroński, M. P., Labiano, A., et al. 2010, MNRAS, 408, 2261
Kuraszkiewicz, J., Wilkes, B. J., Schmidt, G., et al. 2009, ApJ, 692, 1143
Maccagni, F. M., Morganti, R., Oosterloo, T. A., et al. 2018, A&A, 614, A42
Maccagni, F. M., Santoro, F., Morganti, R., et al. 2016, A&A, 588, A46
Madsen, K. K., Beardmore, A. P., Forster, K., et al. 2017, AJ, 153, 2
Marinucci, A., Bianchi, S., Fabbiano, G., et al. 2017, MNRAS, 470, 4039
Marinucci, A., Risaliti, G., Wang, J., et al. 2012, MNRAS, 423, L6
Markoff, S., Falcke, H., & Fender, R. 2001, A&A, 372, L25
Markoff, S., Nowak, M. A., & Wilms, J. 2005, ApJ, 635, 1203
Marshall, H. L., Chen, Y., Drake, J. J., et al. 2021, AJ, 162, 254
Moravec, E., Svoboda, J., Borkar, A., et al. 2022, A&A, 662, A28
Mukherjee, D., Wagner, A. Y., Bicknell, G. V., et al. 2018, MNRAS, 476, 80
O'Dea, C. P., Mu, B., Worrall, D. M., et al. 2006, ApJ, 653, 1115

O'Dea, C. P., & Saikia, D. J. 2021, A&ARv, 29, 3
O'Sullivan, E., Ponman, T. J., & Collins, R. S. 2003, MNRAS, 340, 1375
Orienti, M., & Dallacasa, D. 2008, A&A, 487, 885
Ostorero, L., Moderski, R., Stawarz, Ł., et al. 2010, ApJ, 715, 1071
Ostorero, L., Morganti, R., Diaferio, A., et al. 2017, ApJ, 849, 34
Papachristou, M., Dasyra, K. M., Fernández-Ontiveros, J. A., et al. 2021, AN, 342, 1160
Polatidis, A. G., & Conway, J. E. 2003, PASA, 20, 69
Ponti, G., Terrier, R., Goldwurm, A., et al. 2010, ApJ, 714, 732
Principe, G., Di Venere, L., Orienti, M., et al. 2021, MNRAS, 507, 4564
Principe, G., Migliori, G., Johnson, T. J., et al. 2020, A&A, 635, A185
Readhead, A. C. S., Kiehlmann, S., Lister, M. L., et al. 2021, AN, 342, 1185
Remillard, R. A., & McClintock, J. E. 2006, ARA&A, 44, 49
Ruan, J. J., Anderson, S. F., Eracleous, M., et al. 2019, ApJ, 883, 76
Santoro, F., Rose, M., Morganti, R., et al. 2018, A&A, 617, A139
Siemiginowska, A., Sobolewska, M., Migliori, G., et al. 2016, ApJ, 823, 57
Snellen, I. A. G., Schilizzi, R. T., Miley, G. K., et al. 2000, MNRAS, 319, 445
Sobolewska, M., Migliori, G., Ostorero, L., et al. 2022, ApJ, 941, 52
Sobolewska, M., Siemiginowska, A., Guainazzi, M., et al. 2019a, ApJ, 871, 71
Sobolewska, M., Siemiginowska, A., Guainazzi, M., et al. 2019b, ApJ, 884, 166
Sobolewska, M. A., Siemiginowska, A., & Gierliński, M. 2011, MNRAS, 413, 2259
Stawarz, Ł., Ostorero, L., Begelman, M. C., et al. 2008, ApJ, 680, 911
Sutherland, R. S., & Bicknell, G. V. 2007, ApJS, 173, 37
Tingay, S. J., Macquart, J.-P., Collier, J. D., et al. 2015, AJ, 149, 74
Trichas, M., Green, P. J., Constantin, A., et al. 2013, ApJ, 778, 188
Tschager, W., Schilizzi, R. T., Röttgering, H. J. A., et al. 2000, A&A, 360, 887
van Breugel, W., Miley, G., & Heckman, T. 1984, AJ, 89, 5
Verner, D. A., Ferland, G. J., Korista, K. T., et al. 1996, ApJ, 465, 487
Wagner, A. Y., Bicknell, G. V., & Umemura, M. 2012, ApJ, 757, 136
Wójtowicz, A., Stawarz, Ł., Cheung, C. C., et al. 2020, ApJ, 892, 116
Wu, Q. 2009, ApJL, 701, L95
Yaqoob, T. 2012, MNRAS, 423, 3360
Zovaro, H. R. M., Sharp, R., Nesvadba, N. P. H., et al. 2019, MNRAS, 484, 3393